

REPORT DOCUMENTATION PAGE					<i>Form Approved OMB No. 0704-0188</i>	
The public reporting burden for this collection of information is estimated to average 1 hour per response, including the time for reviewing instructions, searching existing data sources, gathering and maintaining the data needed, and completing and reviewing the collection of information. Send comments regarding this burden estimate or any other aspect of this collection of information, including suggestions for reducing the burden, to Department of Defense, Washington Headquarters Services, Directorate for Information Operations and Reports (0704-0188), 1215 Jefferson Davis Highway, Suite 1204, Arlington, VA 22202-4302. Respondents should be aware that notwithstanding any other provision of law, no person shall be subject to any penalty for failing to comply with a collection of information if it does not display a currently valid OMB control number.						
PLEASE DO NOT RETURN YOUR FORM TO THE ABOVE ADDRESS.						
1. REPORT DATE (DD-MM-YYYY) 31 March 2010		2. REPORT TYPE Final Report		3. DATES COVERED (From - To) 29 September 2009 – 31 March 2010		
4. TITLE AND SUBTITLE Snapshot Raman Spectral Imager				5a. CONTRACT NUMBER W911NF-09-C-0153		
				5b. GRANT NUMBER		
				5c. PROGRAM ELEMENT NUMBER		
6. AUTHOR(S) B. D. Guenther				5d. PROJECT NUMBER		
				5e. TASK NUMBER		
				5f. WORK UNIT NUMBER		
7. PERFORMING ORGANIZATION NAME(S) AND ADDRESS(ES) Applied Quantum Technologies, Inc. Cedar Terrace Office Suites 3333 Durham Chapel Hill Blvd Durham, NC 27707				8. PERFORMING ORGANIZATION REPORT NUMBER		
9. SPONSORING/MONITORING AGENCY NAME(S) AND ADDRESS(ES) US Army Research Office PO Box 12211 4300 S. Miami Blvd Research Triangle Park NC 27709-2211				10. SPONSOR/MONITOR'S ACRONYM(S)		
				11. SPONSOR/MONITOR'S REPORT NUMBER(S)		
12. DISTRIBUTION/AVAILABILITY STATEMENT Approved for public release; distribution unlimited						
13. SUPPLEMENTARY NOTES						
14. ABSTRACT Report developed under topic #A09A-T009, contract W911NF-09-C-0153. Applied Quantum Technologies along with its university partner Duke University conducted, during a Phase I STTR contract, the design of a coded-aperture snapshot Raman imager. The snapshot system design provides dwell times much shorter than conventional slit-based or tunable-filter based spectral imagers. A deep ultra-violet or short-wave infrared excitation source allows for minimal sample fluorescence, making the system able to cope with target signatures in a wide variety of backgrounds. While the majority of Raman systems available are point-based, having imaging capabilities permits wide area coverage at a fraction of the time of point-based systems. By utilizing compressed sensing algorithms, large amounts of spatial and spectral information can be acquired using the limited pixel counts available in detector arrays.						
15. SUBJECT TERMS STTR Report, Raman Spectroscopy, snapshot imager, coded aperture						
16. SECURITY CLASSIFICATION OF:			17. LIMITATION OF ABSTRACT	18. NUMBER OF PAGES	19a. NAME OF RESPONSIBLE PERSON	
a. REPORT	b. ABSTRACT	c. THIS PAGE			B.D. Guenther	
U	U	U	UU	22	19b. TELEPHONE NUMBER (Include area code) 919-403-0926	

Reset

Contractor: Applied Quantum Technologies, Inc.
Contract Number: W911NF-09-C-0153
CLIN: 0001Af
Period of Performance: 01 March 2010 – 31 March 2010

Table of Contents

Forward	3
Statement of the problem studied.....	3
Summary of the most important results.....	3
Phase I Accomplishments	3
Laser Source	6
Solar Background	7
Imaging Detectors	8
System Measurement Model.....	10
Imaging Spectrometer Design.....	11
Related Work.....	17
Bibliography	21

Tables

Table 1: Raman cross-section of common explosives	4
Table 2 Raman cross-sections of common nerve agents	5
Table 3: Sample Parameters.....	5
Table 4: Parameters for Laser Sources for the UV and NIR/SWIR	6
Table 5: Source Parameters	7
Table 6: Background parameters for 1064 nm excitation.....	8

Table 7: NIR/SWIR	9
-------------------------	---

Table 8: UV Detectors	10
-----------------------------	----

Figures

Figure 1: Solar Radiation Spectrum at the earth's surface	8
-----------------------------------------------------------------	---

Figure 2: Single disperser typical design	12
-------------------------------------------------	----

Figure 3 DUV Spectrograph Design.....	12
---------------------------------------	----

Figure 4 Spot diagram at 3 wavelengths and 9 field positions of DUV CASSI spectrograph	14
----------------------------------------------------------------------------------------------	----

Figure 5: (a) Spatial variation in test spectral image, computing by summing intensity across all spectral bands. (b) Spectral image estimate computed using our multiscale EM algorithm for the proposed Phase I architecture.	16
--------------------------------------------------------------------------------------------------------------------------------------------------------------------------------------------------------------------------------------	----

Figure 6: (a) Target spectrum corresponding the white diamond shaped target; blue plot is the true target spectrum and the red plot is the estimate. (b) Target spectrum corresponding the gray star shaped target; blue plot is the true target spectrum and the red plot is the estimate.	16
--------------------------------------------------------------------------------------------------------------------------------------------------------------------------------------------------------------------------------------------------------------------------------------------------	----

Figure 7: Reconstruction error as a function of the number of parallel dual disperser elements.	16
------------------------------------------------------------------------------------------------------	----

Figure 8: Reconstruction errors for various layouts of the FPA corresponding to different configurations of parallel dual disperser systems.	17
---------------------------------------------------------------------------------------------------------------------------------------------------	----

Figure 9 Upper-left- assembled SWIR snapshot multispectral camera system, Upper right- calibration image from detector array, Bottom- reconstructed data-cube of outdoor scene.	18
--------------------------------------------------------------------------------------------------------------------------------------------------------------------------------------	----

Figure 10 AQT's Long-wave Infrared Coded Aperture Spectrometer, Upper-left Real-time software interface providing control, data display, and data storage, Upper-right Comparison of slit (top graph) and coded-aperture (bottom graph) spectral estimates of the transmission spectrum of polystyrene, Bottom- Photographs of assembled system.	19
-------------------------------------------------------------------------------------------------------------------------------------------------------------------------------------------------------------------------------------------------------------------------------------------------------------------------------------------------------	----

Figure 11 Reconstructed data cube of a leaf from a visible range CASSI system	20
-------------------------------------------------------------------------------------	----

Figure 12: (Left) Raw data from a CASSI image of a leaf (Middle) Single frame reconstruction at one spectral channel (Right) 5-frame reconstruction at one spectral channel using multi-frame processing	21
----------------------------------------------------------------------------------------------------------------------------------------------------------------------------------------------------------------	----

Forward

Report developed under topic #A09A-T009, contract W911NF-09-C-0153. Applied Quantum Technologies along with its university partner Duke University conducted, during a Phase I STTR contract, the design of a coded-aperture snapshot Raman imager. The snapshot system design provides dwell times much shorter than conventional slit-based or tunable-filter based spectral imagers. A deep ultra-violet or short-wave infrared excitation source allows for minimal sample fluorescence, making the system able to cope with target signatures in a wide variety of backgrounds. While the majority of Raman systems available are point-based, having imaging capabilities permits wide area coverage at a fraction of the time of point-based systems. By utilizing compressed sensing algorithms, large amounts of spatial and spectral information can be acquired using the limited pixel counts available in detector arrays.

Statement of the problem studied

Applied Quantum Technologies along with its university partner Duke University conducted, during a Phase I STTR contract, the design of a coded-aperture snapshot Raman imager. The snapshot system design provides dwell times much shorter than conventional slit-based or tunable-filter based spectral imagers. A deep ultra-violet or short-wave infrared excitation source allows for minimal sample fluorescence, making the system able to cope with target signatures in a wide variety of backgrounds. While the majority of Raman systems available are point-based, having imaging capabilities permits wide area coverage at a fraction of the time of point-based systems. By utilizing compressed sensing algorithms, large amounts of spatial and spectral information can be acquired using the limited pixel counts available in detector arrays.

In our designs we considered two applications guided by the input from the following Army Scientists: Wayne Antesberger - NVESD, Frank DeLucia – ARL/Aberdeen, Henry Everitt – AMSRD, and Augustus W. Fountain – Edgewood Arsenal. The applications considered in the design and modeling effort were: a SWIR explosives detection for countermines/IED and a UV explosive and biohazard detection system. To estimate the feasibility of a DUV or SWIR system, four critical parameters were evaluated: Raman photon generation, imaging sensor characteristics, excitation laser characteristics, and solar background.

Summary of the most important results

Phase I Accomplishments

- Created a list of absolute cross-sections for several Raman bands in common explosives and nerve agents.
- Found suitable near infrared (SWIR) and deep ultraviolet (DUV) laser sources for the Raman Imager.
- Compared Raman photons generated in the SWIR and the DUV by available laser sources.
- Calculated the number of background photons in sunlight that established the background limited signal to noise in the Raman Imager.
- Compared performance of commercially available SWIR and DUV imaging detectors.
- Selected DUV Raman Imager based on comparison of expected signal to noise of the examined systems.

- Optical designs of a dual disperser and a single disperser were generated and the single disperser was selected for the final optical design.
- A MATLAB simulator was created to model the performance of the optical architecture.
- The simulator was used to evaluate the performance of the reconstruction algorithms and the impact of multiplexing of data.
- An analysis of the impact of noise on the performance of the imaging spectrometer was conducted.

Raman Detection Model:

To model Raman radiation received from an object at a range r at wavelength of λ_0 , we use the equation

$$P(z, \lambda_R) = C_L \frac{\beta_R(z, \lambda_0)}{z^2} \exp\left\{-\int_0^z [\alpha_m(z', \lambda_0) + \alpha_p(z', \lambda_0) + \alpha_m(z', \lambda_R) + \alpha_p(z', \lambda_R)] dz'\right\}$$

where β_R is the Raman backscatter coefficient,

$$\beta_R(\lambda_0, z) = N_R(z) \frac{d\sigma_R}{d\Omega}(\lambda_0, \theta)$$

λ_0 is the laser wavelength, λ_R is the Raman scattered wavelength, α is the extinction coefficient, θ is the scattering angle, m indicates molecular effects and p is scattering by particles. There is also elastic scattered light (Rayleigh) in the return given by

$$P(z, \lambda_0) = C_L \frac{\beta_m(z, \lambda_0) + \beta_p(z, \lambda_0)}{z^2} \exp\left\{-2\int_0^z [\alpha_m(z', \lambda_0) + \alpha_p(z', \lambda_0)] dz'\right\}$$

The absolute cross-sections of several Raman bands of common explosives are given in Table 1.

Table 1: Raman cross-section of common explosives

Explosive	UN		TATP		PETN	RDX	TNT
$K_R \text{ cm}^{-1}$	1050	1010	2992	889	1290	887	1340
$\lambda_0 \text{ nm}$	Cross section $\sigma [\text{cm}^2/\text{molecule} \times \text{sr}]$						
248	8.7×10^{-28}	---	9.9×10^{-29}	2.4×10^{-29}	1.0×10^{-28}	---	9.8×10^{-29}
266	2.2×10^{-28}	---	5.3×10^{-29}	1.9×10^{-29}	3.4×10^{-29}	$\leq 1.0 \times 10^{-32}$	4.3×10^{-29}
355	1.6×10^{-29}	3.6×10^{-30}	9.9×10^{-30}	3.9×10^{-30}	8.6×10^{-30}	7.0×10^{-31}	6.0×10^{-30}
500	---	---				4.1×10^{-31}	
520	5.2×10^{-30}	8.0×10^{-31}	2.0×10^{-30}	6.0×10^{-31}	3.5×10^{-30}		6.0×10^{-31}
532	3.9×10^{-30}	7.1×10^{-31}	8.2×10^{-30}	6.8×10^{-31}	1.7×10^{-30}	9.4×10^{-32}	4.9×10^{-31}
625	6.8×10^{-31}	3.1×10^{-31}	3.8×10^{-31}	3.4×10^{-31}	8.0×10^{-31}	5.0×10^{-32}	2.0×10^{-31}
	Wavelength enhancement- actual versus non-resonant model						
K_{R248}/K_{R625}	1279.4	---	260.5	70.6	125.0	---	490.0
$(625/248)^4$	40.3	40.3	40.3	40.3	40.3	40.3	40.3

Table 2 Raman cross-sections of common nerve agents

Nerve Agent	GA	GB	GD	GF	DIMP
$K_R \text{ cm}^{-1}$	2195	724	729+751	758	718
$\lambda_0 \text{ nm}$	Cross section $\sigma [\text{cm}^2/\text{molecule} \times \text{sr}]$				
248	1.025×10^{-27}	2×10^{-28}	3.35×10^{-28}	2.35×10^{-28}	2.52×10^{-28}
262	3×10^{-28}	1.3×10^{-28}	1.6×10^{-28}	1.55×10^{-28}	---
363.8	5.3×10^{-29}	3.2×10^{-29}	---	---	4.3×10^{-29}
457.9	1.8×10^{-29}	3.2×10^{-29}	---	---	1.4×10^{-29}
488	1.3×10^{-29}	8.0×10^{-30}	---	---	1.3×10^{-29}
514.5	7.5×10^{-30}	5.9×10^{-30}	---	---	7.3×10^{-30}
785	1.5×10^{-30}	1.5×10^{-30}	1.5×10^{-30}	1.0×10^{-30}	1.3×10^{-30}
	Wavelength enhancement- actual versus non-resonant model				
K_{R248}/K_{R785}	683.3	133.3	223.3	235.0	193.8
$(785/248)^4$	100.4	100.4	100.4	100.4	100.4

From the data in Table 2, we selected a prototypical molecule, the nerve agent GA (Tabun), with the following molecular parameters, Table 3, for use in our modeling calculations:

Table 3: Sample Parameters

Parameter	Units	UV Value	SWIR Value
Molecular Weight	Daltons (g/mole)	140.1	140.1
Liquid Density	g/cm^3	1	1
Molecular Density	Molecules/ cm^3	4.30×10^{-21}	4.30×10^{-21}
Penetration Depth	mm	0.1	0.1
Illuminated Area	cm^2	6.25×10^{-6}	6.25×10^{-6}
Molecules illuminated	Molecular density area	4.30×10^{-19}	4.30×10^{-19}
Excitation Wavelength	nm	248	1064
Raman cross section	$\text{cm}^2/\text{sr}/\text{molecule}$	1.03×10^{-27}	4.44×10^{-31}
Raman Generation Probability	Fraction	4.41×10^{-8}	1.91×10^{-11}

The laser wavelengths were chosen to allow for a fluorescence-free background by either going into the deep-UV, or into the short-wave infrared. The combination of the $1/\lambda^4$ scaling of the Raman cross-section and the pre-resonance enhancement provides a 2300x increase in the Raman photon generation probability for the molecule GA. Assuming no pre-resonant

enhancement would lead to a 338x increase in probability.

Laser Source

The excitation wavelength of a Raman system is critical, and there have been many studies comparing the performance of systems at different wavelengths. Near-infrared diode lasers (785-850 nm) are frequently used in laboratory Raman settings due to the decreased fluorescence of longer wavelength excitation, however many chemicals encountered in real-world environments like paint can exhibit strong fluorescence with NIR excitation.¹ Fourier-transform Raman spectroscopy with 1064 nm excitation is a well-developed technique that is free of fluorescence by the longer choice of wavelength--- moving the Raman spectra to the red side of the sample fluorescence.² The other way to reduce sample fluorescence is to go into the deep-UV, hence moving the Raman spectra to the blue side of the fluorescence emission. Work at Brookhaven National Laboratory has established the need to go below 250 nm to ensure a fluorescence-free background for a variety of substrates and interferents.³

A thorough market survey of both NIR/SWIR and DUV lasers was conducted to determine the best combination of sensitivity, power, and size. NIR/SWIR diode lasers have very high efficiencies; however their inability to be pulsed without severely reducing their average power levels makes them difficult to cope with the background solar radiation will be discussed later. Q-switched solid-state lasers at 1064 nm have high peak powers, however their pulse energies are <1 mJ for portable systems (power draw < 100 W, weight <10 kg). Giant-pulse lasers for laser-induced breakdown spectroscopy have high pulse energies, but their extreme weight and power requirements make them not suitable for portable applications. In the DUV the two laser types used for Raman are hollow cathode gas lasers and excimer lasers. The excimers have very high energy pulses, but the gas changing requirements and bulky power supplies needed to power them make them not appealing for this application. The hollow-cathode lasers from Photon Systems Inc. have a low power output compared to the NIR/SWIR lasers, however the increased Raman scattering efficiency and reduced solar background makes them an appealing choice for portable systems.

Table 4: Parameters for Laser Sources for the UV and NIR/SWIR

NIR/SWIR				
Lasers	Wavelength nm	Output W	Input W	Weight kg
Edmund Optics NTS 371	785	0.45	10	1.1
Edmund Optics NTS 372	808	0.45	10	1.1
Edmund Optics NTS 373	976	0.45	10	1.1
PD-LD Luxx Master	976	2	5.6	1
Crystal Laser QIR-1064-1000	1064	1	60	---
Picoquant Nanio	1064	25	1.5×10^3	29
Ultraviolet				

Lasers	Wavelength	Output W	Input W	Weight kg
Photon Systems	248	0.5 mW	10	3.6
Coherent Sabre MotoFreD	248.2	300 mW	55×10^3	311

From the list of available sources, Table 4, the design model was given the following set of source parameters, Table 5, showing the increased ability of the DUV system to generate Raman photons for the chemical analyzed earlier.

Table 5: Source Parameters

Parameter	Units	Photon Systems DUV Laser	Crystal Laser NIR/SWIR Laser
Pulse Power	mW	0.5	1.5×10^6
Pulse Width	μsec	40	0.02
Pulse Energy	μJ	20	300
Beam Diameter	mm	3	3
Wavelength	nm	248.6	1064
Energy/photon	W	8.00×10^{-19}	1.86×10^{-19}
Flux	Photons/pulse	2.5×10^{13}	1.61×10^{15}
Raman photons generated for sample parameters of Table 3	Raman photons/pulse	1.10×10^6	3.08×10^4
Total Power Consumption	W	10	40

Solar Background

The Raman spectrum must be detected in the presence of sunlight thus a key parameter analyzed is the level of background solar radiation in the two spectral bands being investigated, Figure 1. We estimate the background level of sunlight in the optical bandwidth of the expected Raman signal. Table 6 gives the parameters used to establish the background parameters used to evaluate the background-limited signal to noise.

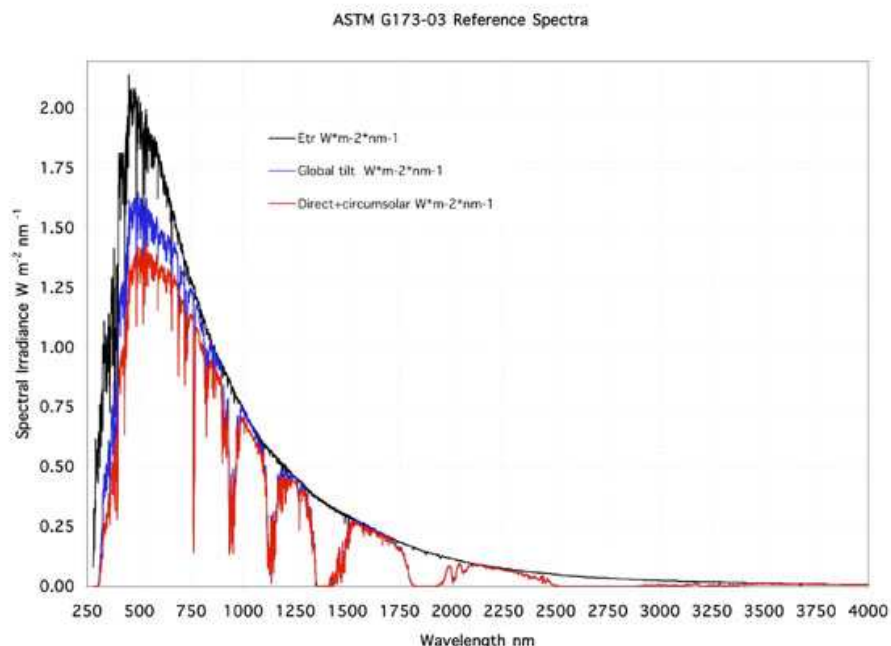


Figure 1: Solar Radiation Spectrum at the earth's surface⁴

From Table 6 the number of background photons generated is comparable to the NIR/SWIR Raman photon generation of Table 4 for a 1 cm^2 area. For point-based systems where the laser would be focused to a diffraction-limited spot, this amount of background could be tolerated. However, for our imaging requirements, the amount of solar radiation would severely hinder the coverage area and the dynamic range of the instrument.

Table 6: Background parameters for 1064 nm excitation

Parameter	Units	Value
Spectral Energy Density	$\text{W/m}^2/\text{nm}$	0.6
Bandwidth	nm	0.5
Energy	W/m^2	0.3
Rayleigh Scattering	Scattering efficiency	0.01
Background Photon Density	$\text{Photons/cm}^2/\text{sec}$	1.6×10^{12}
Background Photons/pulse (20 ns)	$\text{Photons/cm}^2/\text{pulse}$	3.21×10^4

Imaging Detectors

The standoff nature of the proposed system creates a difficult detection problem, as the spectral region of the proposed system is in one of the atmospheric transmission bands of the

short-wave infrared (SWIR). Due to the low efficiency of the Raman scattering process, the background radiation can overwhelm the weak Raman signal. The UV range is appealing in this regard as upper atmospheric absorption by oxygen and ozone eliminate almost all radiation in the Raman shifted range of a 248 nm excitation source.

In order to increase the ratio of Raman to background signal, time gating can be used. By using a pulsed laser and detection system, this ratio can be increased by many orders of magnitude. Detector array systems have been analyzed in the Phase I feasibility study for the NIR/SWIR and UV, Table 8 and Table 7. In the NIR/SWIR a non-intensified Indium-Gallium-Arsenide (InGaAs) focal plane array is the most common technology, and one company makes an intensified detector array using an Indium Phosphide (InP)/InGaAs photocathode. The non-intensified cameras are a more mature technology, but have a disadvantage in that the data must be readout with each pulse of the excitation laser. The readout noise of the camera will severely impact the sensitivity of the system. By averaging multiple shots this effect can be reduced, however the signal still must be relatively strong to do this.

Intensified cameras have two advantages over non-intensified cameras--- amplification of photoelectrons before they are readout by circuitry, and the ability to gate the accumulation of photoelectrons. In the UV a variety of intensified cameras are produced by Andor, Hamamatsu, and Princeton Instruments with excellent readout noise statistics and cooling options, shown in Table 8. The only intensified NIR/SWIR camera that was found that would work with 1064 excitation had no cooling making multiple pulse averaging on the sensor not feasible.

Table 7: NIR/SWIR

NIR/SWIR								
Cameras/Sensors	Pixels	Pixel Size μm	Well Capacity ke^-	Readout Noise e^-	Dark Current $\text{e}^-/\text{pixel/s}$	QE % @ 1100 nm	NEI ($\text{p}/\text{cm}^2/\text{s}$)	DR dB
Hamamatsu S10747-0909	512x512	24x24	200ke-	30		20		76
Noblepeak Triwave CC701	640x480	10x10		7			3.5×10^9	59
Intevac LIVAR 500	640x480	12x12		---	1×10^6	25	1×10^6	
FLIR SC2500	320X256	30	3500	150	150	70		
Goodrich SU640SDWH-1.7RT	640x480	25x25	800	300		65	2.5×10^9	68
Xenics Xeva 1.7-640	640x512	20x20		7-14 A/D counts				
Xenics Xeva2.5320	320x256	30x30		6 A/D counts				

Table 8: UV Detectors

UV						
Cameras/Sensors	Pixels	Pixel Size μm	Well Capacity ke^-	Readout Noise e^-	Dark Current $\text{e}^-/\text{p/s}$	QE % @ 250 nm
Hamamatsu S10141-1109S	2048x506	12x12	75	4	50 (0 C)	50
Intevac Microvista UV	1280x1024	10.8x10.8	40	30	150	45
Sarnoff CAM512-UV	512x512	18x18		100		65
Alta E42-UV	2048x2048	13.5x13.5	100	10	200	60
Andor DV420-UV	1024-255	26x26	465	4		65
Andor DH712	512X512	24x24		4	1	27

The high gain (1000) and low-noise (equivalent background radiation of 0.06 photoe-/s) of the Andor DH712 allows for much higher sensitivity detection than by any of the NIR/SWIR cameras. The detector array performance combined with the higher Raman photon generation rate, smaller power supply requirements, and lack of solar background radiation, led to the decision to pursue a DUV-based system.

System Measurement Model

New system models were explored to address two issues of previous CASSI designs--- spatial/spectral resolution trade-offs, and computation time. In a CASSI system, a limited number of multiplexed measurements of an unknown data-cube are used to infer the entire data-cube by exploiting the sparsity of the data-cube on some mathematical basis. The compression ratio of the system--- ratio of measurements made to data-cube elements reconstructed, is limited by things like the noise in the measurement system, and the degree of sparsity in the data-cube. The resultant system still has a limited number of spatial and spectral channels, resulting in limited spatial and spectral resolutions. In Raman spectroscopic applications, the high spectral resolution required makes the implementation of a snapshot CASSI system problematic.

Initially, the use of a multi-aperture CASSI system was proposed as a way to increase the spatial and spectral resolution of the system. By providing a more diverse set of projections of the data-cube, it was estimated that system performance would be increased. This was the measurement model that was investigated by the University subcontractor.

A number of issues with the multi-aperture approach were identified during the system modeling feasibility analysis:

- 1) Reduced system aperture- the weak nature of Raman scattering requires a large

aperture size to provide enough photons for the imaging detectors. Having a multi-aperture system with large (4-6") apertures is not feasible due to the size, weight, and cost of the optic, along with the difficulty of routing all of the light to a single focal plane.

2) Limited pixel count- large pixel count arrays were not found to be available in the spectral ranges (UV and SWIR) required to be in a fluorescence-free region, limiting the final system spatial and spectral resolutions.

A more appealing approach that will be used in Phase II is the use of multi-resolution, multi-frame processing model. The snapshot processing approach will be implemented along with a multi-frame processing approach that will be used to enhance the spatial and spectral resolution of the resultant output. The system will be able to provide rapid scanning of an area with coarse resolution, which can then be enhanced by taking multiple images of a region of interest with the CASSI platform dithering or a slight movement of the coded-aperture. Some initial work done at Duke University using this approach is shown in the Related Work section.

Imaging Spectrometer Design

There are two frequently used disperser designs that can be implemented in a CASSI system:

Dual Disperser: A dual disperser design where the source is imaged through two sequentially dispersive arms arranged in opposition so that the dispersion in the second arm cancels the dispersion introduced by the first arm. A coded aperture is placed between the two arms. Recovery of the datacube from the detector measurement is performed using an expectation-maximization method designed for hyperspectral images. Such a design applies spatially varying, spectral filter functions with narrow features. Through these filters, the detector measures a spectral projective measurement of the datacube. The dual disperser sacrifices spatial information to gain spectral information about the datacube. The use of multiple dispersers reduces the sensitivity of the total system due to the increased number of optical elements and also increases the alignment requirements of the system. A useful property of the design is that the measurement resembles the scene, making it easy to focus the camera on objects in the scene.

Single Disperser: A single disperser coded aperture snapshot imaging spectrometer, as shown in Figure 2,

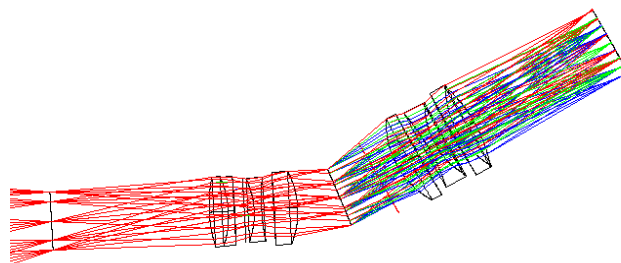
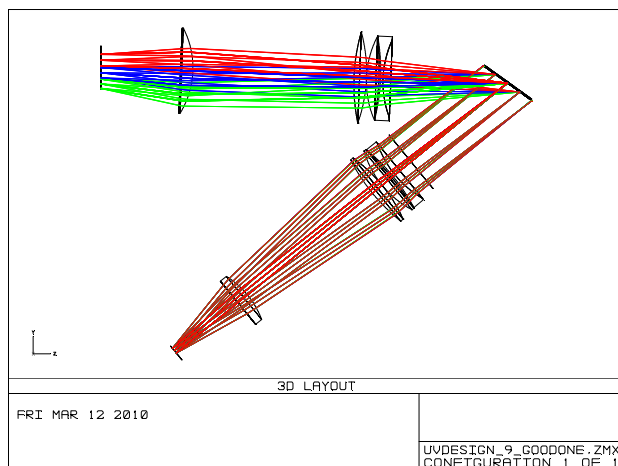


Figure 2: Single disperser typical design

consists of an imaging lens that illuminates the aperture code and a pair of relay lenses that relay the image from the plane of the aperture code to the detector through a dispersive element placed between them. The single disperser does not directly measure each voxel in the desired three-dimensional datacube. It collects a small number (relative to the size of the datacube) of coded measurements and a sparse reconstruction method is used to estimate the datacube from the noisy projections. The instrument disperses spectral information from each spatial location in the scene over a large area across the detector; thus, spatial and spectral information from the scene is multiplexed on the detector. A raw measurement of a scene on the detector rarely reveals spatial structure of the scene and makes block processing more challenging. The use of a single disperser increases the sensitivity of the system and is our choice for initial designs.

The conclusion drawn from the design and modeling conducted during Phase I was to limit our attention in Phase II to the design and construction of a UV Raman imager based on Coded-Aperture Snapshot Spectral Imaging (CASSI) technology. The CASSI technology offers two possible disperser designs a dual disperser, and a single disperser. Initial designs focused on a dual disperser design, which was used for the signal processing modeling, however the underlying math can be translated to a single disperser approach in Phase II with minimal effort. Modeling of system performance conducted in Phase I has led us to select the single disperser design for the Phase II prototype.

A specific DUV design is shown in Figure 3, which uses a standard 4200 lines/mm grating from Richardson gratings and custom spherical optics (2 sets of 4) made of fused silica and calcium fluoride, two glasses that have high transmission in the DUV. The total system footprint is 75x100 mm with 1" optics and an f/number of 2.8 with good image quality over a 3x3 mm field.

*Figure 3 DUV Spectrograph Design*

The spot diagram of the lens design is shown in Figure 4, and the spot radii are almost all between 5 and 10 microns, providing adequate optical resolution for most of the intensified UV cameras that have pixel sizes between 10 and 25 microns.

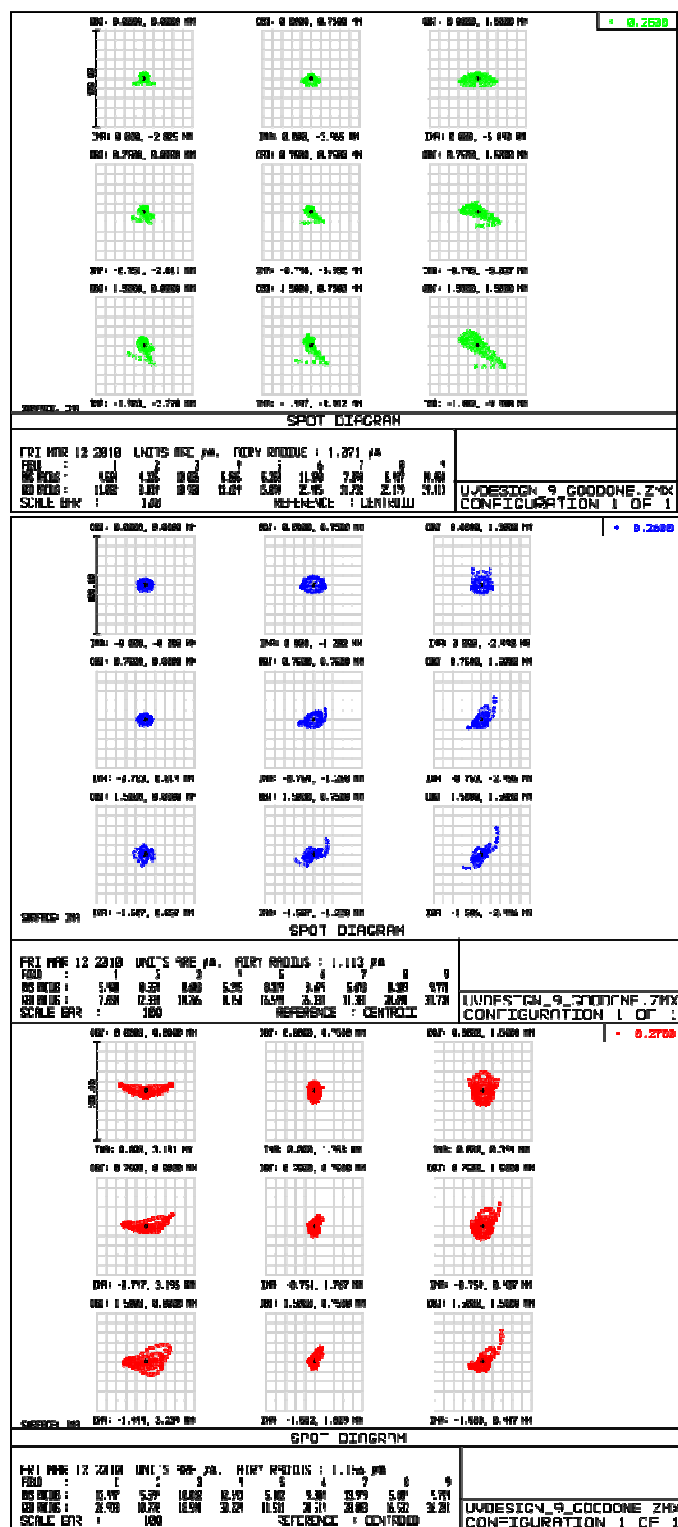


Figure 4 Spot diagram at 3 wavelengths and 9 field positions of DUV CASSI spectrograph

Signal Processing:

In Phase I, we developed a MATLAB simulation framework to model the proposed optical architecture and test reconstruction procedures. Our model allowed us to

- vary the size of the focal plane array and explore how many measurements should be necessary to achieve a given level of reconstruction accuracy;
- vary the number of multiplexed dual disperser elements to explore how multiplexing impacted the tradeoff between spectral and spatial resolution;
- vary the amount of photon and sensor noise contaminating the measurements; and
- experiment with different coding masks.

Our first task was to develop a mathematical model relating the true spectral image of the scene to the measurements, which would be collected under the proposed system architecture. In particular, the model needed to be flexible enough to allow us to simulate how different parameters in the architecture (i.e. the size of the focal plane array, the number of dual disperser elements, the amount of light available, and the selection of the coding masks) might impact performance. From a linear algebra standpoint, we can write our model as follows. Let \mathbf{f} be a vectorized representation of the spectral image, so that if the spectral image is $n_1 \times n_2 \times n_3$, then \mathbf{f} is a length- $n_1 n_2 n_3$ vector. Let \mathbf{y} be the measurements collected by the m -element focal plane array and stored in a length- m vector. Then we have

$$\mathbf{y} \sim \mathcal{P} \left(\underbrace{\begin{bmatrix} H_1 \\ H_2 \\ \vdots \\ H_k \end{bmatrix}}_H \mathbf{f} \right) + \mathbf{n}$$

where k is the number of parallel dual disperser elements, H_i , $i = 1, 2, \dots, k$, are the operators describing the projections of \mathbf{f} onto the i^{th} coding mask for the corresponding dual disperser system and subsampling onto the FPA, \mathbf{n} denotes (Gaussian) sensor noise, \mathcal{P} denotes Poisson observations (i.e. photon noise), and H is the overall system operator matrix.

In order to reconstruct the high-resolution input intensity \mathbf{f} from the observations \mathbf{y} , we developed an iterative expectation-maximization algorithm based on state-of-the-art multiscale methods for reconstruction spectral images.

$$[\text{E-step:}] \mathbf{x}^{(t)} = \hat{\mathbf{f}}^{(t)} \cdot \mathbf{H}^T (\mathbf{y} / \mathbf{H} \hat{\mathbf{f}}^{(t)}).$$

$$[\text{M-step:}] \text{Compute } \hat{\mathbf{f}}^{(t+1)} = \text{Denoise}(\mathbf{x}^{(t)}).$$

For the M-step, we performed the translation-invariant denoising approach that we developed to recover spectral image intensities from Poisson observations. This approach is based on the key insight that the spatial boundaries stay the same in every spectral band even though the photon flux may vary with every spectral band.

For our numerical experiments, we developed a test spectral image based on the spectra in⁵. The input intensity \mathbf{f} is of size $256 \times 256 \times 64$ and the sum (along the spectral dimension)

through the test input spectral image appeared as in Figure 5a. Two of the spectra from this test spectral image are displayed in Figure 6 in the blue plots. Figure 5b and the red plots in Figure 6 show the result of our method applied to a simulated system with 16 parallel dual dispersers, each with a unique pseudo-random coding mask and mapping to a 64×64 region of the focal plane array.



Figure 5: (a) Spatial variation in test spectral image, computed by summing intensity across all spectral bands. (b) Spectral image estimate computed using our multiscale EM algorithm for the proposed Phase I architecture.

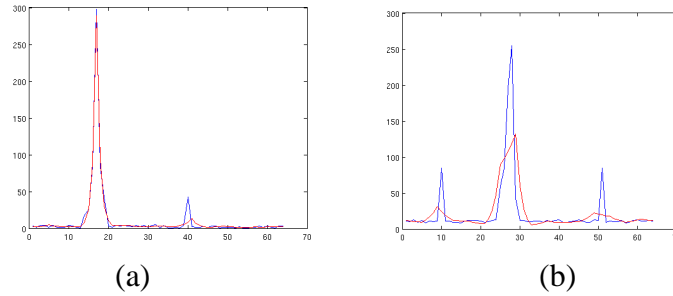


Figure 6: (a) Target spectrum corresponding the white diamond shaped target; blue plot is the true target spectrum and the red plot is the estimate. (b) Target spectrum corresponding the gray star shaped target; blue plot is the true target spectrum and the red plot is the estimate.

We also explored how performance scaled with the number of dual disperser systems, k , as shown in Figure 7. In this experiment, each dual disperser element mapped to a 64×64 region on the FPA, so more dual dispersers implies more observations. Thus the error should naturally decay with k , though after $k=8$ we reach a point of diminishing returns.

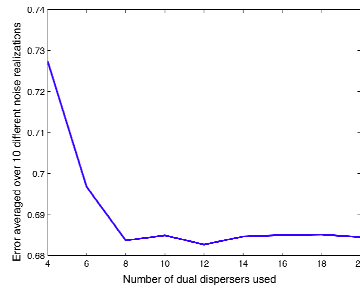


Figure 7: Reconstruction error as a function of the number of parallel dual disperser elements.

We also considered holding the FPA size fixed at 256 x 256, and then varying k , so that larger k implies fewer observations per dual disperser element. We considered the configurations displayed in Figure 8, which also contains the reconstruction errors achieved using our algorithms.

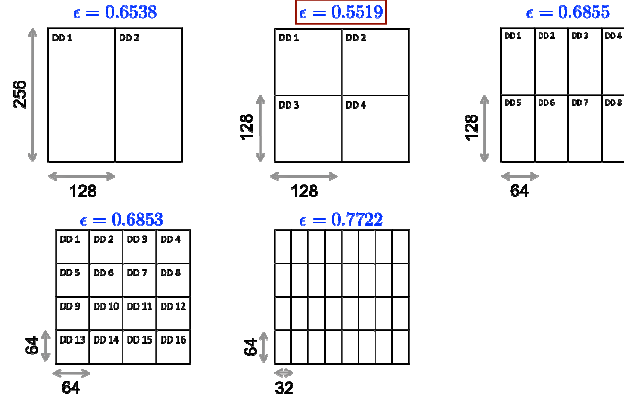


Figure 8: Reconstruction errors for various layouts of the FPA corresponding to different configurations of parallel dual disperser systems.

The image processing that is an integral part of the snapshot Raman Imager must be implemented on a graphics processing unit (GPU) to demonstrate the utility of the imager for field applications. We have developed a processing algorithm that will be generated in standard Matlab code to be run on any NVIDIA CUDA-capable GPU, from the GeForce 8400 to the Tesla C1060.

Related Work

Applied Quantum Technologies designed, built, and delivered a snapshot multispectral short-wave infrared (SWIR) camera in 2008 to a leading defense contractor. The camera was able to recover 10 spectral bands equally spaced from 1-1.7 microns using a coded-aperture and compressive sampling inference algorithms. An optical design similar to what will be the starting point for the proposed design was used. A 3-element prism provided the dispersion for the system, and off-the-shelf lenses were used in the spectrograph. A Goodrich SWIR camera served as the detector array. The system, along with a calibration image and reconstructed data-cube is shown in **Figure 9**. The main issues with the final system were that the off-the-shelf optics were poorly chromatically corrected, and that the reconstruction software was very slow (>1 minute). Both of these issues are prime focuses of the Phase I design effort.

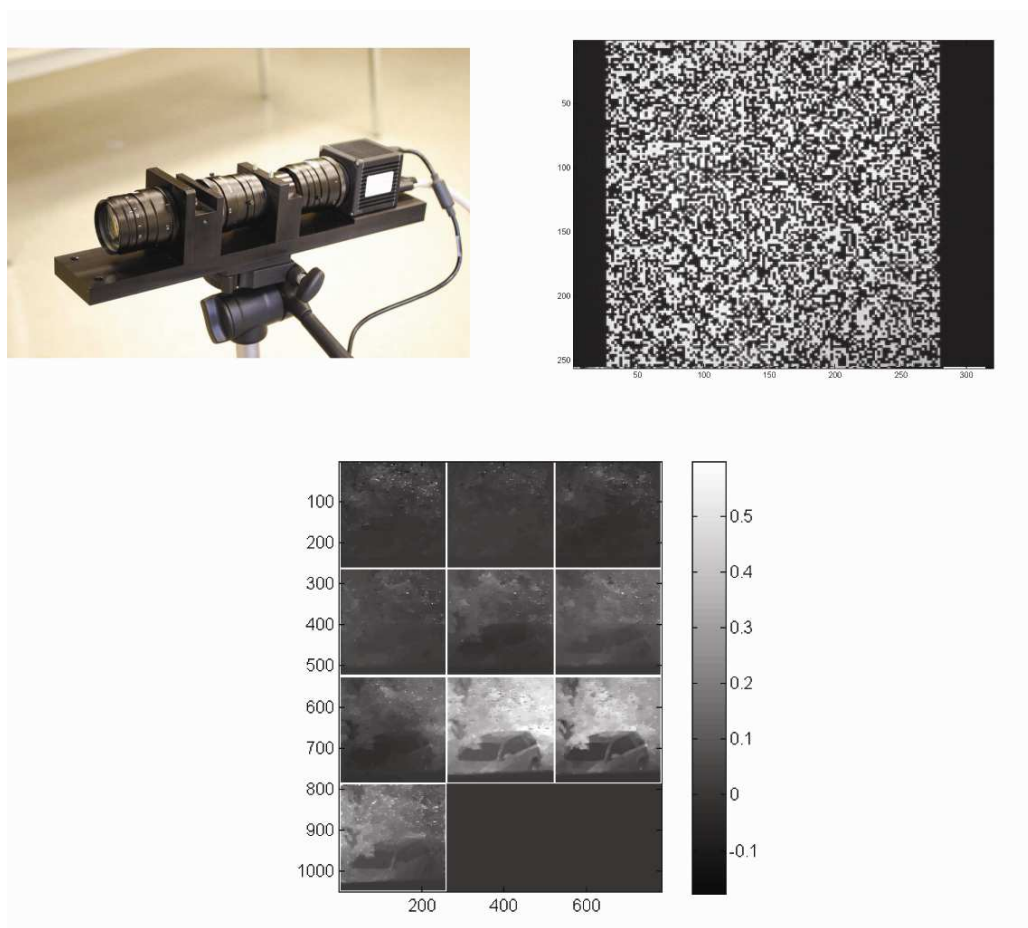


Figure 9 Upper-left- assembled SWIR snapshot multispectral camera system, Upper right- calibration image from detector array, Bottom- reconstructed data-cube of outdoor scene.

AQT has also recently (2009) delivered a prototype long-wave-infrared (LWIR) coded-aperture spectrometer to a customer for remote chemical analysis. The customer wanted to replace a bulky Fourier-Transform Infrared (FTIR) system with a dispersive system to lower the cost and size of the instrument. AQT used a coded-aperture to increase the throughput without sacrificing resolution, as is shown in the comparison between the coded-aperture data and slit data in Figure 10. A near real-time software interface, also shown, was developed in Labview that was able to process the imagery from the camera at 30 frames per second with a lag of under 1 second.

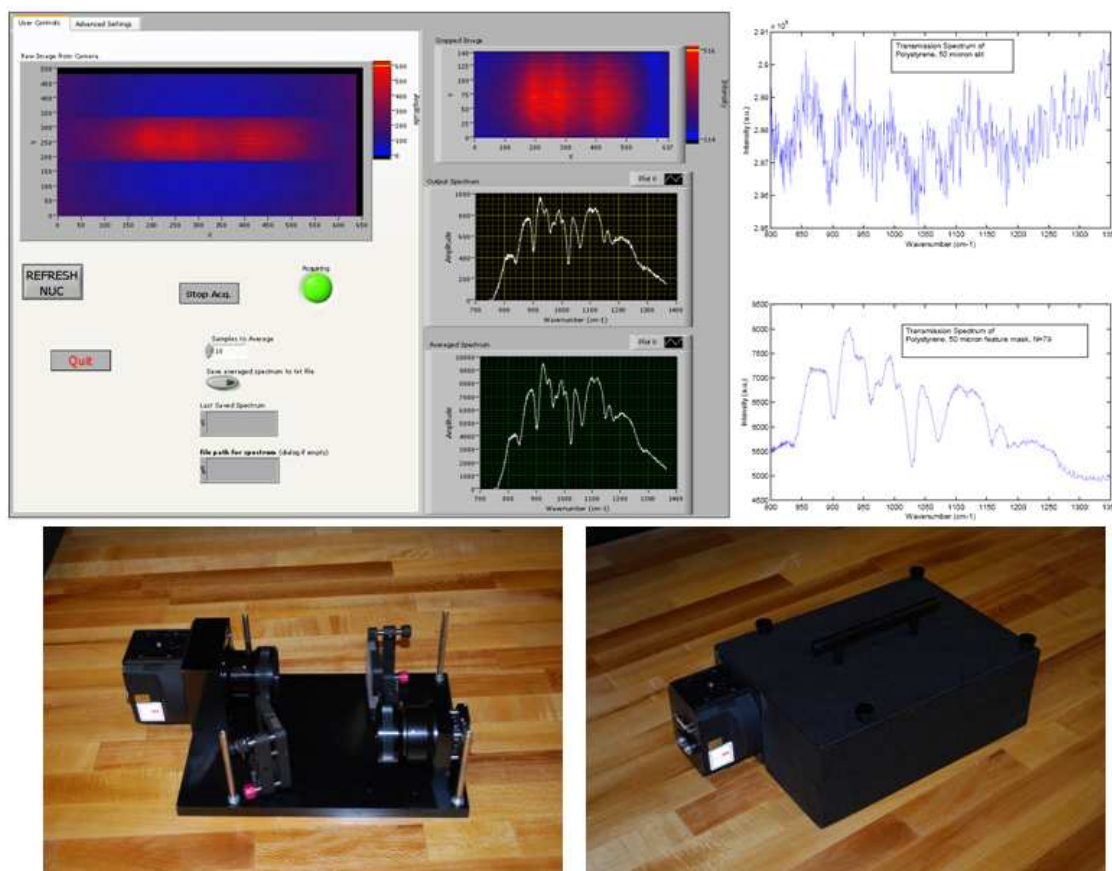


Figure 10 AQT's Long-wave Infrared Coded Aperture Spectrometer, Upper-left Real-time software interface providing control, data display, and data storage, Upper-right Comparison of slit (top graph) and coded-aperture (bottom graph) spectral estimates of the transmission spectrum of polystyrene, Bottom- Photographs of assembled system.

Dr. David Brady, a consultant on the project, is investigating multi-frame analysis of CASSI systems for enhanced resolution capabilities. This will allow for better resolution in the spatial and spectral dimensions, and allow for accurate object tracking within a field of view. Multiple frame processing is based on slight (pixel level) displacements in image registration due to object or camera motion and jitter. Initial studies with a visible CASSI system have demonstrated that datacube estimation using just a few frames may substantially improve image fidelity. Figure 11, as an example, is a 27 channel CASSI image of a white light-illuminated leaf processed using 5 frames acquired from pixel-scale camera translation. Figure 12 shows raw CASSI data for the leaf from a single frame. Dispersion of the CASSI code, appearing as noise on the raw data, encodes spectral information on the monochromatic sensor data. Comparisons of single frame and five-frame reconstructions for specific wavelength channels are shown in Figure 12.

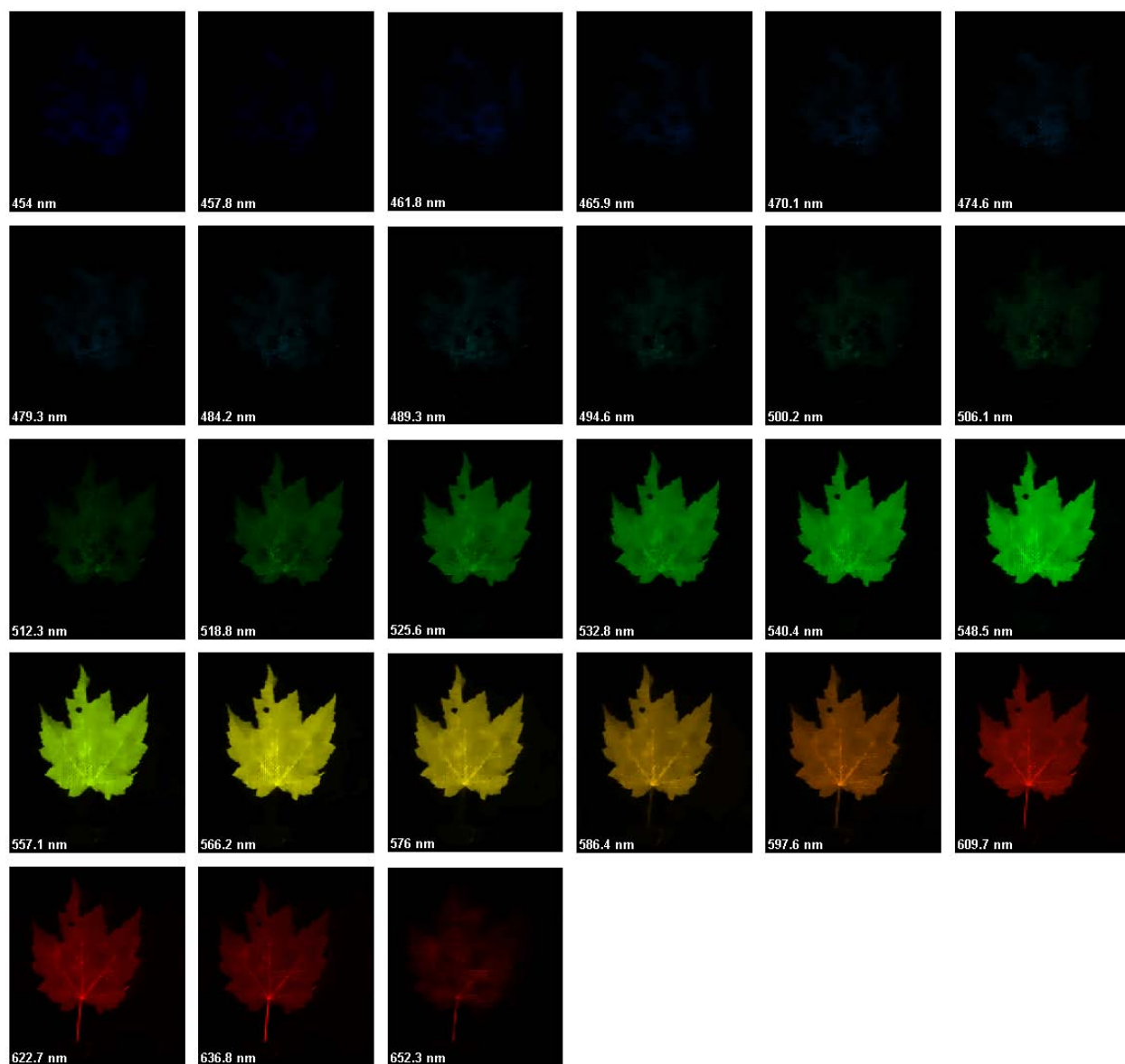


Figure 11 Reconstructed data cube of a leaf from a visible range CASSI system

As illustrated in these figures estimation of spectral images from the space-time image data cube improves CASSI spatial resolution. In contrast with conventional scanned spectral imagers, however, CASSI returns a full data cube even from a single frame and allows incremental and adaptive image improvement by space-time processing. This function is particularly important in applications requiring real-time rapid spectral scanning, and the advances by Dr. Brady's research group at Duke University will be evaluated for possible integration into the Phase 2 effort.

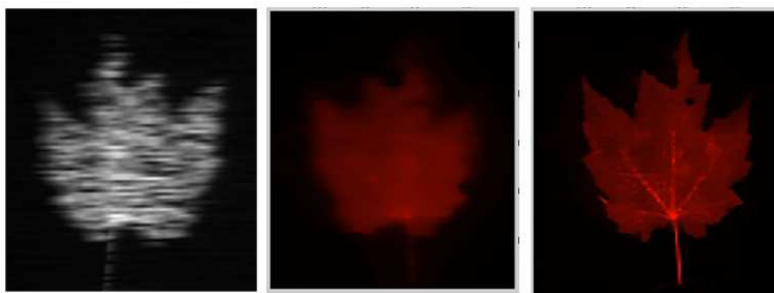


Figure 12: (Left) Raw data from a CASSI image of a leaf (Middle) Single frame reconstruction at one spectral channel (Right) 5-frame reconstruction at one spectral channel using multi-frame processing

The Duke signal processing team has performed a significant body of research intimately connected to the research described in this proposal. First, we have established fundamental performance bounds for compressed sensing^{6,7,8} and associated optimization algorithms^{9,10} for image reconstruction from photon-limited compressive measurements. The key insight underlying these methods was that conventional CS measurements are not amenable to most optical or IR systems because of positivity and flux preservation constraints. Unlike most previous work in CS, we considered non-negative projections, limited photon counts, Poisson noise models, and limited FPA sizes. Second, we have studied photon-limited spectral intensity estimation and proposed a spatially- and spectrally-adaptive, nonparametric method to estimate spectral intensities from Poisson observations¹¹. Upper bounds on the error of our estimator match the best possible lower bound up to a log factor for certain degrees of spatial and spectral smoothness. Finally, we have developed algorithms to exploit inter-frame correlations in video data for improved reconstruction accuracy and speed.^{12,13}

Bibliography

¹ M. Gaft, L. Nagli, “Standoff laser-based spectroscopy for explosives detection,” Proceedings of the SPIE, Volume 6739, pp. 673903 (2007).

² P.J. Hendra, C. Jones, G. Warnes, Fourier Transform Raman Spectroscopy: Instrumentation and Chemical Applications, Ellis Horwood, Chichester, UK, 1991. Chapter 5, pp. 90-126.

³ Sedlacek III, A.J.; Ray, M.D.; Higdon, N.S.; Richter, D.A. Short-range noncontact detection of surface contamination using Raman lidar *Proc. SPIE.* **2001**, 95, 4577.

⁴ American Society for Testing and Materials (ASTM) Terrestrial Reference Spectra for Photovoltaic Performance Evaluation, <http://rredc.nrel.gov/solar/spectra/am1.5/#refs>

⁵ P. J. Treado, M. P. Nelson, R. Schweitzer, C. Gardner, and R. Wentworth, "Standoff Raman Hyperspectral Imaging Detection of Explosives," in *Laser Applications to Chemical, Security and Environmental Analysis*, 2008.

⁶ S. Jafarpour, R. Willett, M. Raginsky, and R. Calderbank. "Performance bounds for expander-based compressed sensing in the presence of Poisson noise". In Forty-Third Asilomar Conference on Signals, Systems and Computers, 2009. Winner of best student paper award.

⁷ M. Raginsky, Z. T. Harmany, R. F. Marcia, and R. Willett. "Performance bounds for compressed sensing with Poisson noise". *IEEE Trans. on Signal Proc.*, 2009. Submitted.

⁸ R. Willett and M. Raginsky. "Performance bounds for compressed sensing with Poisson noise". In *Proc. of IEEE Int. Symp. on Inf. Theory*, 2009.

⁹ Z. Harmany, R. Marcia, and R. Willett. "Sparse Poisson intensity reconstruction algorithms". In *Proc. IEEE Workshop on Statistical Signal Processing*, 2009.

¹⁰ R. Marcia, R. Willett, and Z. Harmany. "Compressive optical imaging: Architectures and algorithms". To appear in *Optical and Digital Image Processing Fundamentals and Applications*, edited by G. Cristobal, P. Schelkens and H. Thienpont, 2010.

¹¹ K. Krishnamurthy, M. Raginsky, and R. Willett. "Multiscale photon-limited hyperspectral image reconstruction," submitted to *SIAM Journal on Imaging Sciences*, 2010.

¹² R. Marcia, C. Kim, J. Kim, D. Brady, and R. Willett. "Superimposed video disambiguation for increased field of view", *Optics Express*, vol. 16, no. 31, 16352-16363.

¹³ R. Marcia and R. Willett. "Compressive Coded Aperture Video Reconstruction", European Signal Processing Conference — EUSIPCO 2008.